Magnetism out of antisite disorder in the J=0 compound Ba_{2}YIrO_{6}

Q. Chen, C. Svoboda, Q. Zheng, B. C. Sales, D. G. Mandrus, H. D. Zhou, J.-S. Zhou, D. McComb, M. Randeria, N. Trivedi, and J.-Q. Yan

Phys. Rev. B **96**, 144423 — Published 18 October 2017
DOI: 10.1103/PhysRevB.96.144423

Magnetism out of antisite disorder in a $J = 0$ compound Ba_2YIrO_6

Q. Chen,[1] C. Svoboda,[2] Q. Zheng,[3] B. C. Sales,[3] D. G. Mandrus,[3, 4] H. D. Zhou,[1] J.-S. Zhou,[5] D. McComb,[6] M. Randeria,[2] N. Trivedi,[2, *] and J.-Q. Yan[3, †]

[1]*Department of Physics and Astronomy, University of Tennessee, Knoxville, Tennessee 37996, USA*
[2]*Department of Physics, The Ohio State University, Columbus, OH 43210, USA*
[3]*Materials Science and Technology Division, Oak Ridge National Laboratory, Oak Ridge, Tennessee 37831, USA*
[4]*Department of Materials Science and Engineering,*
University of Tennessee, Knoxville, Tennessee 37996, USA
[5]*Materials Science and Engineering Program, University of Texas at Austin, Austin, Texas 78712, USA*
[6]*Department of Materials Science and Engineering,*
The Ohio State University, Columbus, OH 43210, USA

We systematically investigate the magnetic properties and local structure of Ba_2YIrO_6 to demonstrate that Y and Ir lattice defects in the form of antiphase boundary or clusters of antisite disorder affect the magnetism observed in this d^4 compound. The experimental investigation involved comparison of the magnetic properties and atomic imaging of (1) a slow-cooled crystal, (2) a crystal quenched from 900°C after growth, and (3) a crystal grown using a faster cooling rate during growth than the slow-cooled one. Atomic-scale imaging by scanning transmission electron microscopy (STEM) shows that quenching from 900°C introduces Ir-rich antiphase boundaries in the crystals, and a faster cooling rate during crystal growth leads to clusters of Y and Ir antisite disorder. Compared to the slow-cooled crystals, Ba_2YIrO_6 crystals with clusters of antisite defects have a larger effective moment and a larger saturation moment, while quenched crystals with Ir-rich antiphase boundary show a slightly suppressed moment. Our DFT and model magnetic Hamiltonian calculations suggest magnetic condensation is unlikely as the energy to be gained from superexchange is small compared to the spin-orbit gap. However, once Y is replaced by Ir in the antisite disordered region, the picture of local non-magnetic singlets breaks down and magnetism can be induced. This is because of (a) enhanced interactions due to increased overlap of orbitals between sites, and, (b) increased number of orbitals mediating the interactions. Our work highlights the importance of lattice defects in understanding the experimentally observed magnetism in Ba_2YIrO_6 and other $J = 0$ systems.

I. INTRODUCTION

The magnetic properties of octahedrally coordinated Re^{3+}, Ru^{4+}, Os^{4+}, and Ir^{5+} with a d^4 electronic configuration were first studied around 1960s.[1] The large crystal electric field prefers the low spin configuration for these 4d/5d transition metal compounds. The strong spin orbit coupling and the hybridization between transition metal d-orbital and oxygen p-orbital further complicate the magnetic behavior by reducing the magnetic moment or the orbital angular momentum, respectively. In the presence of a strong spin-orbit coupling, a temperature independent magnetic susceptibility is expected.

Both $4d$ and $5d$ transition metal ions in the d^4 (ie. $t_{2g}^4 e_g^0$) configuration are expected to be non-magnetic in both the weakly and strongly correlated limits. In the weakly correlated picture, t_{2g} shells are split into a fully filled $j = 3/2$ shell and an empty $j = 1/2$ shell due to strong spin-orbit coupling. Spin-orbit coupling then opens up a bandgap between the $j = 3/2$ and $j = 1/2$ bands leading to a non-magnetic insulating ground state. In the strongly correlated picture, the first two Hund's rules require each d^4 site to be in a total $S = 1$ and total $L = 1$. Strong spin-orbit coupling then yields a local $J = 0$ state on every ion. Again the ground state is non-magnetic.

Interest in d^4 magnetism was revived after a report of long range magnetic order in Sr_2YIrO_6[2] and the proposal of a condensation mechanism for magnetism in d^4 Mott insulators.[3] It was predicted that the hopping of electrons between neighboring sites would lead to an exchange interaction that could compete with the onsite spin-orbital singlet and generate a local moment.[4] The anomalous magnetic moments observed in A_2YIrO_6 (A=Sr, and Ba) double perovskites and the fragile magnetism in $R_2Os_2O_7$ (R=rare earth) have been the subject of intense theoretical and experimental investigations.[2–15] A fundamental question still remains: what is the root cause of the anomalous magnetism in these $5d^4$ compounds?

There are two prominent explanations which have been applied to these $5d^4$ materials. The first explanation is quenching of the orbital degrees of freedom through octahedral distortions. Uniaxial distortions (ie. $\delta(\boldsymbol{L} \cdot \hat{n})^2$) split the t_{2g} orbitals into an orbital singlet and an orbital doublet. When the orbital doublet is lower in energy, the doublet is filled and the singlet is empty, and the conclusion is still a non-magnetic ground state. However if the orbital singlet is lower in energy, it is occupied by two electrons while the other two electrons occupy the doublet. This half filled orbital doublet then has a total spin $S = 1$ leading to a magnetic ground state. Cao et. al.[2] proposed this distortion mechanism was the cause of the $0.9\ \mu_B$/Ir moments and the long range magnetic order at $1.3\,K$ in Sr_2YIrO_6. However studies on $Ba_{2-x}Sr_xYIrO_6$ where the lattice distortion was tuned by varying the x

found the moment shows little dependence on the chemical pressure. This leads to the conclusion that octahedral distortions are not responsible for moment formation.[7,10] It is also worth mentioning that Dey et. al.[9] and Corredor et. al.[11] observed no long range magnetic order in Ba_2YIrO_6 and Sr_2YIrO_6 crystals down to 0.4 K despite the presence of magnetic moments.

The second explanation is a theoretical mechanism for “excitonic” condensation proposed by Khaliullin[3] which is generally applicable to strongly spin-orbit coupled d^4 systems. Each Ir^{5+} ion is nominally in a local non-magnetic $J = 0$ state with an energy gap of $\lambda/2$ to the next lowest energy state of $J = 1$ where λ is the spin-orbit coupling strength appearing as $(\lambda/2)\boldsymbol{L}\cdot\boldsymbol{S}$. For very small superexchange interactions, the system remains in its unperturbed product state of non-magnetic $J = 0$ singlets, but large superexchange interactions can result in a second-order phase transition to a magnetic ground state. Superexchange effectively allows a $J = 1$ excitation to move between sites giving it a k-space dispersion $\omega(\boldsymbol{k})$. The bandwidth of this dispersion is directly proportional to the superexchange coupling constant t^2/U where t is the hopping and U is the on-site Coulomb repulsion. As the bandwidth of $\omega(\boldsymbol{k})$ increases, the energy gap between non-magnetic $J = 0$ product state and excited $J = 1$ states is reduced until the gap closes at a critical value of $(t^2/U)/\lambda$ where the condensation of these magnetic excitations occurs.

Despite the observation of Curie moments in both Sr_2YIrO_6 and Ba_2YIrO_6, density functional theory calculations have lead to contradictory results. Initially, Bhowal et. al.[5] performed GGA+SOC+U calculations within the plane wave basis to find antiferromagnetic (AFM) ground states in both Sr_2YIrO_6 and Ba_2YIrO_6 despite the absence of distortions in cubic Ba_2YIrO_6. However, a later study by Pajskr et. al.[6] rebutted this claim using dynamical mean field theory (DMFT) to obtain a non-magnetic ground state. Furthermore, this study estimated the gap between the $J = 0$ singlets and the $J = 1$ triplets to be more than 250 meV which marginalizes the prospect of condensation. We will argue on simpler grounds that this finding is qualitatively correct, and the condensation mechanism is not active in Ba_2YIrO_6.

In addition to the above routes to intrinsic magnetism, extrinsic effects remain plausible. Dey et. al.[9] suggested the magnetism in Ba_2YIrO_6 was due to paramagnetic impurities. In a later study[11], they identified a Schottky anomaly in the specific heat of Sr_2YIrO_6 pointing to the conclusion that paramagnetic impurities are responsible for the observed Curie susceptibilities without the onset of long range magnetic order. In this study, we pursue this line of reasoning and examine the magnetic properties of three types of Ba_2YIrO_6 single crystals with different heat treatments. The varied heat treatments provide samples with antiphase boundary or clusters of antisite disorder, which allow us to probe the effect of lattice defects on the magnetic properties. We find that larger effective moments and saturation moments are observed in crystals with Y/Ir antisite disorder as clusters. This correlation suggests that antisite disorder contributes to the observed moments. To investigate the plausibility of magnetic condensation in Ba_2YIrO_6, we develop a microscopic model for the condensation of $J = 1$ triplet excitations in double perovskites. Using tight-binding parameters from DFT, we show a large energy gap between the non-magnetic $J = 0$ ground state and the lowest energy $J = 1$ triplet excitations remains so that the condensation of magnetic excitations should not occur in Ba_2YIrO_6. We then estimate how antisite disorder can contribute to the magnetism in the A_2YIrO_6 double perovskites. In the antisite disordered region, both the overlap of orbitals between sites and the number of orbitals mediating the interaction increase thus enhancing the interactions which break down the picture of local non-magnetic singlets and induce magnetism.

II. EXPERIMENTAL

Ba_2YIrO_6 single crystals were grown out of $BaCl_2$ flux starting with presynthesized polycrystalline Ba_2YIrO_6 materials. The polycrystalline Ba_2YIrO_6 was prepared by the conventional solid-state reaction method. A homogeneous mixture of stoichiometric amount of starting materials $BaCO_3$, IrO_2 and Y_2O_3 with purities not less than 99.9% was pelletized and sintered at 900°C for 6 hours. The pellets were then ground into fine powder, pelletized, and fired at 1050°C for 15 hours. The last sintering was performed at 1200°C for 30 hours with one intermediate grinding. Room temperature x-ray powder diffraction measurement shows that Ba_2YIrO_6 powder synthesized using the above procedure has about 5% Y_2O_3 impurity. The presynthesized Ba_2YIrO_6 powder was then mixed with $BaCl_2$ in a mass ratio 1:20. The homogeneous mixture of charge and flux was kept inside of a 20 ml sized Pt crucible with a cover. The crystal growth was performed using three different cooling processes as illustrated in Fig. 1(a). Ba_2YIrO_6 single crystals were collected after dissolving the $BaCl_2$ flux in hot water.

Room temperature X-ray powder diffraction patterns were collected on a X’Pert PRO MPD X-ray Powder Diffractometer using the Ni-filtered Cu-K_α radiation. The Rietvelt refinement of the diffraction patterns was performed using Fullprof package. The elemental analysis was performed using a Hitachi TM-3000 tabletop electron microscope equipped with a Bruker Quantax 70 energy dispersive x-ray (EDX) system. The elemental analysis does not observe deviation from the desired stoichiometry. Magnetic properties were measured with a Quantum Design (QD) Magnetic Property Measurement System in the temperature interval $1.8\,K \leq T \leq 750\,K$. Thermopower around room temperature was measured in a homemade setup.

Scanning transmission electron microscopy (STEM)

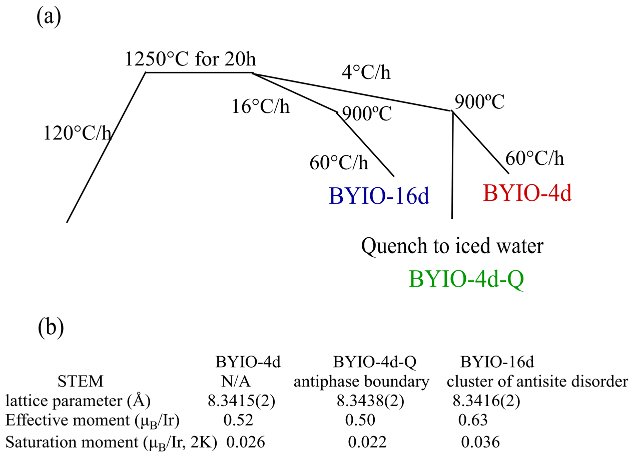

	BYIO-4d	BYIO-4d-Q	BYIO-16d
STEM	N/A	antiphase boundary	cluster of antisite disorder
lattice parameter (Å)	8.3415(2)	8.3438(2)	8.3416(2)
Effective moment (μ_B/Ir)	0.52	0.50	0.63
Saturation moment (μ_B/Ir, 2K)	0.026	0.022	0.036

FIG. 1. (color online) (a) Temperature profiles for the growth of Ba_2YIrO_6 crystals. BYIO-4d: slow-cooled crystal. BYIO-4d-Q: quenched into iced water from 900°C. BYIO-16d: a faster cooling rate (16°C/h) during crystal growth. (b) A summary of defects observed by STEM, lattice parameter, effective moment, and saturation moment at 2K for all three samples.

specimens were prepared by crushing Ba_2YIrO_6 crystals in methanol. Drops of the resulting suspensions were deposited on lacey carbon copper grids and then dried in air. High-angle annular dark-field-STEM (HAADF-STEM) imaging was performed on two aberration-corrected STEM machines, FEI Titan S 80-300 operating at 300 kV (for BYIO-4d and BYIO-4d-Q) with a probe convergence angle of 25.2 mrad and an inner collection angle of 65 mrad, and Nion UltraSTEM 100^{TM} operating at 100 kV (for BYIO-16d) with a probe convergence angle of 30 mrad and an inner collection angle of 86 mrad.[16] All STEM measurements were done at room temperature.

III. RESULTS

A. X-ray powder diffraction and thermopower

With the motivation of investigating the possible effects on magnetism of lattice defects, we grew Ba_2YIrO_6 crystals using different cooling rates as shown in Fig. 1(a). After homogenizing at 1250°C, sample BYIO-4d was cooled down to 900°C at a cooling rate of 4°C per hour and then to room temperature at 60°C per hour. Sample BYIO-4d-Q was quenched in iced water after cooling from 1250°C to 900°C at 4°C per hour. Sample BYIO-16d was cooled from 1250°C to 900°C at 16°C per hour which is followed by cooling to room temperature at 60°C per hour. The slow-cooled BYIO-4d sample can be looked as the reference for the other two samples. Room temperature x-ray powder diffraction measurements of pulversized crystals suggest the presence of Y_2O_3 in all three crystals. The Rietvelt refinement of the diffraction pattern suggests about 2% Y_2O_3 in BYIO-4d sample. This is in line with the observation by Dey et al. The amount of Y_2O_3 increases to 6% in BYIO-4d-Q and 11% in BYIO-16d. Dey et al[9] proposed that the observed Y_2O_3 exists as inclusions in crystals. While this is quite likely, we occasionally observe under optical microscope isolated Y_2O_3 in BYIO-16d. The lattice parameters are a=8.3415(2)$\mathring{A}$, 8.3438(2)$\mathring{A}$, and 8.3416(2)$\mathring{A}$ for BYIO-4d, BYIO-4d-Q, and BYIO-16d, respectively. The different cooling processes do not affect the lattice parameters of the as-grown Ba_2YIrO_6 crystals. In the Rietvelt refinement of each pattern, we also tried to include the antisite disorder. Including about 2% Y/Ir antisite disorder can marginally improve the quality of Rietvelt refinement. However, the refinement suggests all three crystals have the similar amount of antisite order.

One important concern is whether the different cooling processes change the stoichiometry of the resulting crystals. Our EDX measurements do not suggest, in resolution limit, that the different cooling processes lead to any deviation for Ba, Y and Ir from the desired ratio in the resulting crystals. Dye et al. annealed the as-grown Ba_2YIrO_6 crystals under 700 bar oxygen pressure at 500°C for 2 days but did not notice any change to the magnetic properties.[9] This suggests that the amount of oxygen vacancies in the slow cooled crystals, if any, should be negligible and below the detection limit (around 2%) of Thermal Gravity Analysis (TGA) or neutron diffraction. We thus measure the thermopower of our Ba_2YIrO_6 single crystals. All crystals show a temperature independent thermopower about 200 μV/K around room temperature. We also measured the electrical resistivity of dense Ba_2YIrO_6 pellets quenched from 900°C and compared it with that of a slow cooled pellet. Both samples show a resistive behavior with an activation energy of 0.4 eV. The above crystal characterization results (1) suggest that the different growth processes performed in this work do not seem to alter the stoichiometry of the Ba_2YIrO_6 crystals, and (2) allow us to correlate the difference among those three crystals in magnetic properties with their defects revealed by our STEM study.

B. STEM

In the perfect Ba_2YIrO_6 structure, four crystallographic sites are expected to be fully occupied by Ba, Y, Ir, and O, respectively. In fully ordered state, Y and Ir ions order into the rock-salt arrangement. However, this ordered arrangment can be destroyed at antiphase boundary or by antisite disorder where Y cation occupies the position of Ir or vice versa. Heat treatment is an effective approach to tune the degree of the cation order of double perovskites in materials processing. It is expected that the faster cooling during crystal growth and quenching from high temperature might introduce defects such as antisite disorder or antiphase boundary. In order to investigate possible lattice defects induced by

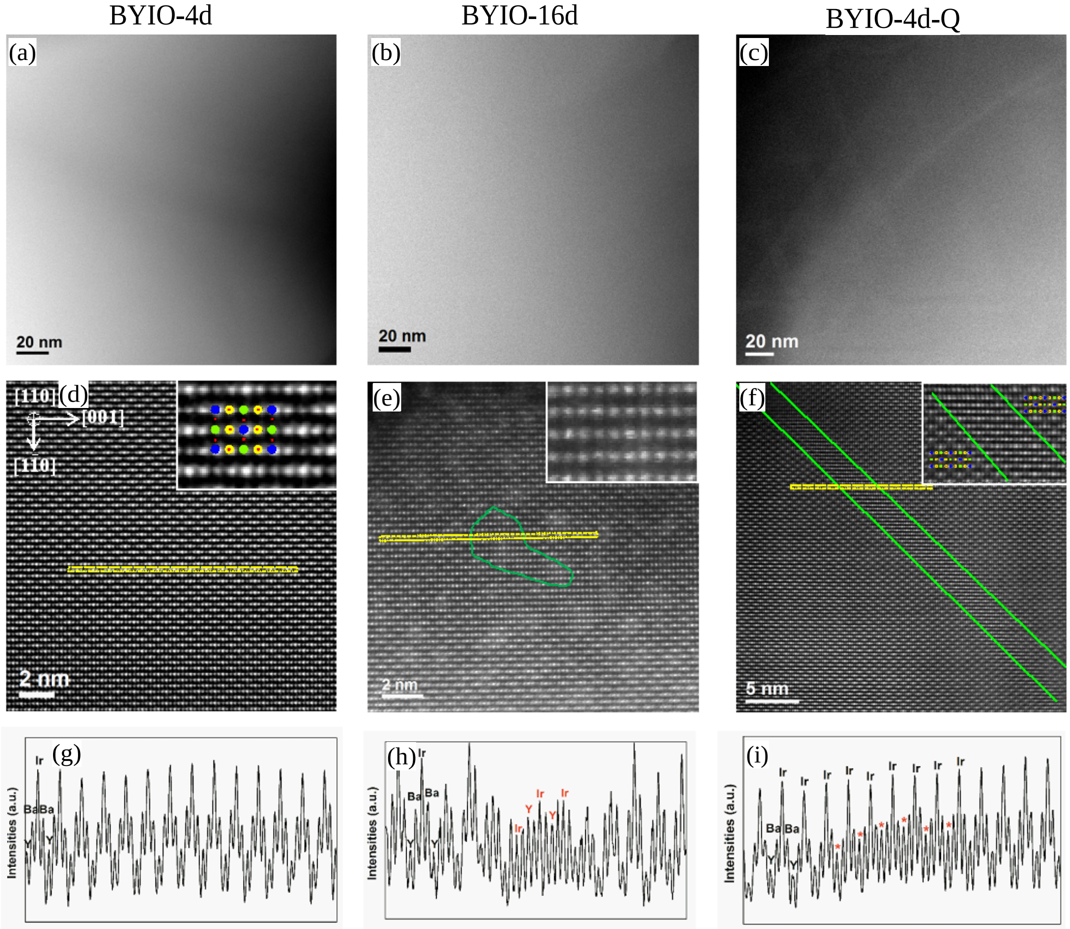

FIG. 2. (Color online) HADDF-STEM images in the [110] projection of Ba_2YIrO_6 crystals. (a, b, c) show the low magnification HAADF image for BYIO-4d, BYIO-16d, and BYIO-4d-Q, respectively. (d, e, f) show the high resolution HAADF image for BYIO-4d, BYIO-16d, and BYIO-4d-Q, respectively. Inset of (d) highlights the ordering in BYIO-4d (yellow: Ba, green: Y, blue: Ir, and red: O). Inset of (e) shows the details of a disordered region of BYIO-16d. Inset of (f) highlights a narrow defected region through the ordered crystal.(g, h, i) show the intensity profile of atomic columns along [001] as marked by the (yellow) lines in (d, e, and f) for BYIO-4d, BYIO-16d, and BYIO-4d-Q, respectively.

quenching from high temperature or fast cooling during crystal growth, we performed STEM on all three samples.

Along [001], Y and Ir atoms are always projected in the same columns. However, three types of cationic columns could be sequentially imaged in the [110] projection with an arrangement of Ba-Y-Ba-Ir-Ba columns. That means imaging along [110] can better reveal atomic-level distribution of the cations, especially the ordering behavior of cations at Y and Ir sites. As shown below, in the [110] projection, Ba, Y, and Ir atoms can be well distinguished by Z contrast. Therefore, STEM is an ideal tool to resolve the microstructural defects that might be related to the observed magnetic moments in Ba_2YIrO_6.

Figure 2(a-f) show the HAADF images along [110] for all three Ba_2YIrO_6 crystals. The low magnification HAADF image for BYIO-4d crystal (see Fig. 2(a)) reveals it is chemically homogenous without any large scale chemical inhomogeneity or structural disorder. This homogeneity is also evidenced by its high-resolution HAADF (HR-HAADF) image as shown in Fig. 2(d). A typical intensity profile of columns (Fig. 2(g)) in this image shows ideal sequential arrangement of Ba-Y-Ba-Ir-Ba columns, and no structural defects are found within the resolution limit of HAADF imaging.

This structural perfection is destroyed when the Ba_2YIrO_6 crystal is grown using a faster cooling rate during crystal growth. While the low magnification HAADF image for BYIO-16d crystal (Fig. 2(b)) does not show any chemical or structural disorder in a large scale, a careful investigation of the high resolution (HR) HAADF image find disordered regions as highlighted by the (green) curves in Fig. 2(e). The intensity profile of columns (Fig. 2(h)) across the disordered region reveals strengthened intensities of Y columns while weakened ones of Ir columns, indicating the appearance of antisite disorder. The largest in-plane dimension of the disordered region can be around 8 nm.

Figure 2(c) shows the low magnification HAADF image for the BYIO-4d-Q crystal quenched from 900°C. Different from the featureless images in Figs. 2(a) and 2(b), a narrow stripe-like region longer than 100 nm can be well observed. As revealed by HR-HAADF image shown in Fig. 2(f), the width of the stripe-like region is around 5 nm. Fig. 2(i) shows the intensity profile across this defected region. The intensity of Y columns becomes stronger in the defected region, while no obvious anomaly is observed for the intensity of Ir columns. This is quite different from that in BYIO-16d where the increased intensity of Y columns is accompanied with the weakened intensity of Ir columns. The difference signals that quenching from 900°C induces one type of defects different from antisite disorder. The dimension of the defected region and the intensity change of Y and Ir columns suggest the formation of an antiphase boundary in the quenched sample BYIO-4Q. The antiphase boundary seems to be Ir-rich with a composition of $Ba_2(Y_{1-x}Ir_x)IrO_6$. Considering possible probe channeling effect,[17] we cannot rule out the possible occupation of Y at Ir site in the antiphase boundary region. However, the population of Y at Ir site, if any, should be small.

Our HAADF-STEM imaging shows that a faster cooling during crystal growth leads to antisite disordered regions with the largest dimension of 8 nm. While quenching from 900°C results in the formation of antiphase boundary of 5 nm wide and over 100 nm long which is Ir-rich. Although in the BYIO-4d crystals, HAADF images show no obvious sign of antisite disorder, we could still reasonably speculate that small disordered regions, such as single site antisite disorder, exist in these crystals, which are however out of the detection limit of HAADF imaging.

C. Magnetic properties

Figure 3 shows the temperature dependence of magnetic susceptibility of BYIO-4d measured in an applied magnetic field of 20 kOe in both field-cooling (FC) and zero-field-cooling (ZFC) modes. FC and ZFC curves overlap in the whole temperature range $2\,\mathrm{K} \leq T \leq 750\,\mathrm{K}$. As reported before, no sign of long range order is observed.[9] The magnetic susceptibility decreases with increasing temperature up to 750 K. This suggests the contribution from the magnetic excited states is small. The susceptibility of a system with a nonmagnetic ground state and a magnetic excited state can be described by[18]

$$\chi(T) = \frac{N_A g^2 \mu_B^2 \nu J(J+1)(2J+1)e^{(-\Delta E/T)}}{3k_B T[1+\nu(2J+1)e^{-\Delta E/T}]} \tag{1}$$

where N_A is the Avogadro number, g is the spectroscopic splitting factor, μ_B is the Bohr magneton, ν is the orbital degeneracy of the excited states, k_B is the Boltzmann constant, ΔE is the energy difference between the nonmagnetic ground state and the magnetic excited state. With $\Delta E = 350\,\mathrm{meV}$,[19] the magnetic susceptibility from the $J = 1$ state is estimated to be 9×10^{-7} emu/mol and has little effect on the temperature dependence of total magnetic susceptibility.

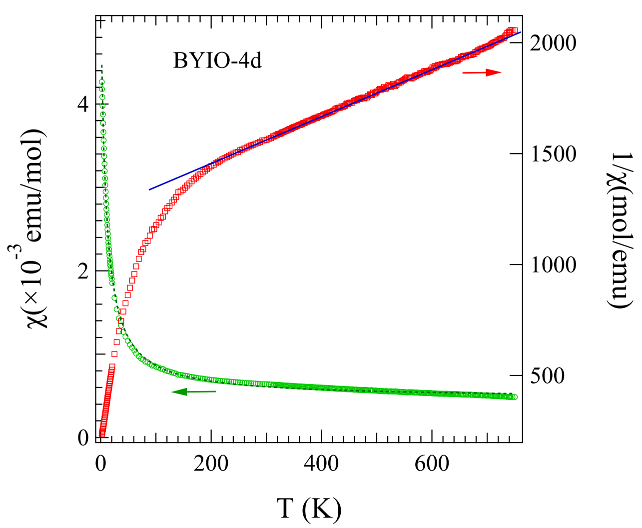

FIG. 3. (color online) Temperature dependence of magnetic susceptibility χ and $1/\chi$ for BYIO-4d single crystals in the temperature range $2\,\mathrm{K} \leq T \leq 750\,\mathrm{K}$ measured in an applied magnetic field of 20 kOe. The solid (blue) line shows the linear fitting of $1/\chi$ above 200 K. The dashed curve shows the fitting with a Curie-Weiss law as described in the text.

Figure 3 also shows the reciprocal of magnetic susceptibility. As highlighted by the solid line, a linear temperature dependence of $1/\chi$ can be found in the temperature range $240\,\mathrm{K} \leq T \leq 750\,\mathrm{K}$. The linear fitting using $1/\chi(T) = (T-\theta)/C$ where C is the Curie constant and θ the Weiss constant, gives an effective moment $\mu_{\mathrm{eff}} = 2.90\,\mu_{\mathrm{B}}$/Ir and a Weiss constant of about -1200 K. Both μ_{eff} and θ are unreasonably large in a system that is nominally comprised of J=0 singlets. As shown by the dashed curve in Fig. 3, the temperature dependence of $\chi(T)$ can be roughly described by adding a temperature independent term χ_0 in the Curie-Weiss fitting $\chi(T) = \chi_0 + C/(T-\theta)$. However, a large χ_0 about 5×10^{-4} emu/mol is needed. This value is comparable to that reported by Dey et al.[9] Before we present the Curie-Weiss fitting results of all samples, we first evaluate whether such a large χ_0 is reasonable.

Three contributions to χ_0 should be considered for Ba_2YIrO_6: the diamagnetic susceptibility from core electrons, χ_{core}, the diamagnetic signal from the sample holder, and the Van Vleck paramagnetic susceptibility, χ_{vv}. By adding the core electron diamagnetic susceptibility of each ion, χ_{core} is found to be -1.68×10^{-4} emu/mol.[9] The diamagnetic signal from the sample holder (straw and capsule) is estimated to be about -1×10^{-4} emu/mol. For the temperature independent χ_{vv}, a simple calculation by standard perturbation the-

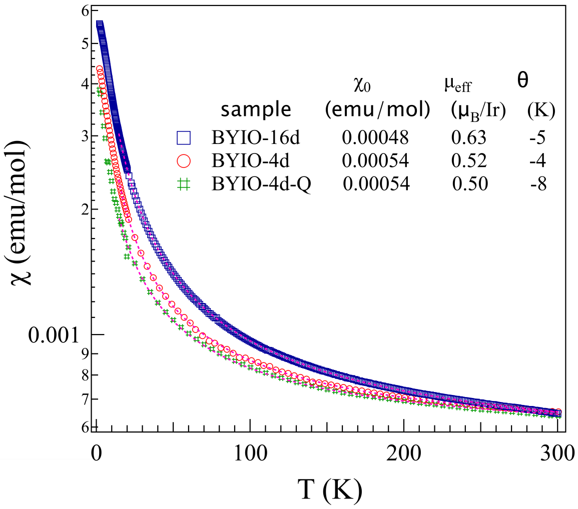

FIG. 4. (color online) Temperature dependence of magnetic susceptibility of Ba_2YIrO_6 single crystals in the temperature range $2\,K \leq T \leq 300\,K$ measured in an applied magnetic field of 50 kOe. The dashed curves show the Curie-Weiss fitting in the temperature range $15\,K \leq T \leq 300\,K$. The fitting parameters are listed in the inset.

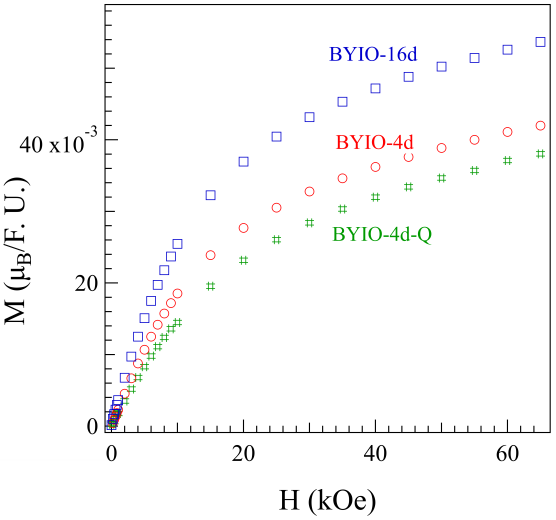

FIG. 5. (color online) Field dependence of magnetization of Ba_2YIrO_6 single crystals at 2 K.

ory gives

$$\chi_{\rm vv} = 2N_A \frac{|\langle j=1|\mu_z|j=0\rangle|^2}{\Delta E} \tag{2}$$

where $\Delta E = 350$ meV according to RIXS data.[19] In the t_{2g}^4 configuration, the magnetic moment operator can be written as $\boldsymbol{\mu} = -i\sqrt{6}(\boldsymbol{T} - \boldsymbol{T}^\dagger - g_J\boldsymbol{J})$, where $g_J = 1/2$. Thus we obtain that[3]

$$\chi_{\rm vv} = \frac{12N_A\mu_{\rm B}^2}{\Delta E} = 11 \times 10^{-4}\text{emu/mol} \tag{3}$$

Therefore, the χ_0 is estimated to be around 8×10^{-4} emu/mol, which is larger than the fitting value of 5 $\times 10^{-4}$ emu/mol. Figure 4 shows the temperature dependence of magnetic susceptibility of all three Ba_2YIrO_6 crystals below room temperature. No sign of long range magnetic order was observed above 2 K. We fit the data in the temperature range $15\,K \leq T \leq 300\,K$ using $\chi(T) = \chi_0 + C/(T-\theta)$. The temperature range $15\,K \leq T \leq 300\,K$ was selected purposely for a direct comparison with the report by Dey et al. The fitting parameters are also listed in Fig. 4. The χ_0 is similar for all three samples. BYIO-4d-Q has the smallest effective moment but the largest Weiss constant. The effective moment for BYIO-16d is over 20% larger than those for BYIO-4d and BYIO-4d-Q.

Figure 5 shows the field dependence of magnetization measured at 2 K. Linear fits to the magnetization versus applied magnetic field data, $M(H)$, for the field range H = 30-65 kOe gives the intrinsic susceptibility from the slope and the saturation magnetization from the $H = 0$ intercept. The intrinsic susceptibility for these three crystals is close to each other, while the saturation magnetization for BYIO-16d is much larger than that for BYIO-4d and BYIO-4d-Q. The saturation magnetization is 0.036, 0.026, and 0.022 $\mu_{\rm B}$/Ir for BYIO-16d, BYIO-4d, BYIO-4d-Q, respectively. The effective moment and saturation moment at 2K are summarized in Fig.1 (b) together with the lattice parameter and defects observed by STEM.

IV. THEORY

A. Condensation Mechanism

We revisit the DFT-DMFT theory results[6] that confirm a non-magnetic ground state. To gain insight into why magnetic condensation is absent, we must connect those results with the condensation mechanism which pits superexchange with an energy scale of t^2/U against the singlet-triplet energy gap of $\Delta_{\rm SOC}$ from spin orbit coupling. The critical ratio of superexchange to spin-orbit coupling required to produce magnetic condensation in a single perovskite[3] is given approximately by $10t^2/U \geq \Delta_{\rm SOC}$. In this section, we will repeat this analysis for double perovskites and find the criteria for closing the singlet-triplet gap.

We first obtain a tight-binding model relevant for Y-Ir double perovskites. The large crystal field splitting induced by $5d$ oxygen octahedral complexes separates the e_g orbitals in energy so that only the t_{2g} orbitals are relevant. Then we can write our tight-binding model as the sum of electron hopping between t_{2g} orbitals in the yz, xz, and xy planes as $H = H_{yz} + H_{xz} + H_{xy}$. For the xy plane, for example, we can restrict the form of the

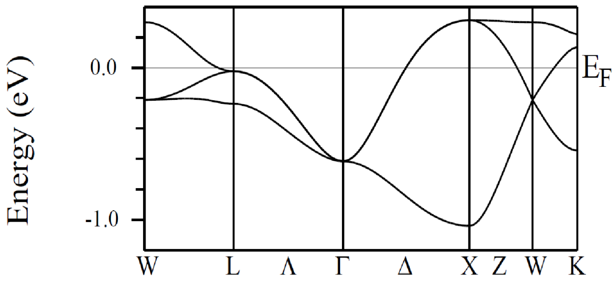

FIG. 6. The GGA band structure *without* spin-orbit coupling is shown. A tight-binding model with t_{2g} Wannier orbitals is fit to the three bands pictured.

tight-binding model by symmetry

$$H_{xy} = \sum_{\langle ij\rangle \in xy} \sum_{\alpha\beta} \sum_{\sigma\in\{\uparrow,\downarrow\}} t_{\alpha\beta}\, c^{\dagger}_{i\alpha\sigma} c_{j\beta\sigma} + \text{h.c.} \tag{4}$$

$$t_{\alpha\beta} = \begin{bmatrix} t_{11} & t_{12} & 0 \\ t_{12} & t_{11} & 0 \\ 0 & 0 & t_{33} \end{bmatrix}_{\alpha\beta} \tag{5}$$

where α and β index the t_{2g} orbitals yz, xz, and xy in this order and $\langle ij\rangle$ ranges over nearest neighbors within an xy plane of the lattice of Ir ions. Next-nearest neighbor hopping is ignored since the resulting superexchange constants will be negligible. (See Appendix B.) We then use a DFT calculation[20] to obtain these tight-binding parameters *without* spin-orbit coupling to separate the energy scales for superexchange and spin-orbit coupling. Fig.6 shows the band structure of the three (t_{2g}) bands.

A tight-binding fit with maximally localized Wannier orbitals[21] yields the following parameters: $t_{11} = +23$ meV, $t_{12} = \pm 19$ meV, and $t_{33} = -131$ meV. Note the value of t_{12} takes a different sign for different pairs of nearest neighbors due to relative orientations of t_{2g} orbitals.

We now calculate the triplet excitation Hamiltonian where triplet excitations from the non-magnetic $J = 0$ to excited $J = 1$ states are described by $|J_i = 1, J_{i,z} = m\rangle = T^{\dagger}_{i,m} |J_i = 0\rangle$. After performing a unitary transformation into cubic coordinates $T_x = \frac{1}{i\sqrt{2}}(T_1 - T_{-1})$, $T_y = \frac{1}{\sqrt{2}}(T_1 + T_{-1})$, and $T_z = iT_0$, the quadratic part of the effective triplet Hamiltonian has the following form

$$H'_{xy} = \sum_{\langle ij\rangle\in xy} \Big[\Big(\boldsymbol{T}^{\dagger}_i \cdot \boldsymbol{A} \cdot \boldsymbol{T}_j + \boldsymbol{T}^{\dagger}_i \cdot \boldsymbol{B} \cdot \boldsymbol{T}^{\dagger}_j + \text{h.c.} \Big) + \Big(\boldsymbol{T}^{\dagger}_i \cdot \boldsymbol{C} \cdot \boldsymbol{T}_i + (i \leftrightarrow j) \Big) \Big] \tag{6}$$

where $\boldsymbol{T}^{\dagger}_i = (T^{\dagger}_{i,x}, T^{\dagger}_{i,y}, T^{\dagger}_{i,z})$ and the matrices $\boldsymbol{A}$, $\boldsymbol{B}$, and $\boldsymbol{C}$ involve combinations of the hopping terms with an overall energy scale proportional to t^2/U; detailed expressions for $\boldsymbol{A}$, $\boldsymbol{B}$, and $\boldsymbol{C}$ are given in the Appendix A. The triplet Hamiltonian for the other two planes can be obtained from cyclic permutations on H'_{xy}. The total Hamiltonian for the triplet excitations is given by the sum over all three planes and the singlet-triplet gap of Δ_{SOC}.

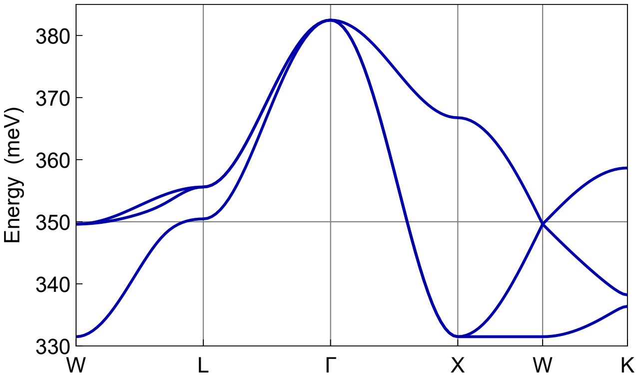

FIG. 7. The triplet excitation spectrum is plotted using a spin-orbit gap of 350 meV. Superexchange reduces the cost to make a triplet excitation at the edge of the Brillouin zone. The lowest energy excitations appear along X-W about 20 meV lower than the original 350 meV spin-orbit gap.

$$H' = H'_{yz} + H'_{zx} + H'_{xy} + \Delta_{\text{SOC}} \sum_i \boldsymbol{T}^{\dagger}_i \cdot \boldsymbol{T}_i \tag{7}$$

To determine when condensation occurs, we diagonalize the effective Hamiltonian H' and obtain the energy dispersion $\omega(\boldsymbol{k})$ for triplet excitations. Before performing the rigorous calculation with all parameters included, it is useful to obtain a simple estimate for the energy scales required to produce magnetic condensation. To obtain this estimate, ignore the superexchange dependent contributions to the singlet-triplet gap (ie. set $\boldsymbol{C} = 0$) and only include the largest tight-binding parameter t_{33} (ie. set $t_{11} = t_{12} = 0$). In this simplified scenario, the $\boldsymbol{A}$ and $\boldsymbol{B}$ matrices are diagonal with $\boldsymbol{A} = -\boldsymbol{B}$, and a closed form solution can easily be obtained. The condition for closing of the singlet-triplet gap is given by the following.

$$\frac{16}{3} \frac{t_{33}^2}{U} \geq \Delta_{\text{SOC}} \tag{8}$$

This value is approximately half of the estimate for single perovskites[3] ($10t^2/U \geq \Delta_{\text{SOC}}$) with the difference due to fewer superexchange paths available in face-centered cubic geometry compared to simple cubic geometry. With a U value taken to be 2 eV, the left-hand side is estimated to be 45 meV compared to the spin-orbit gap of $\Delta_{\text{SOC}} \approx 350$ meV for Ba_2YIrO_6.[19] From this estimate, the condensation mechanism should be inactive in Ba_2YIrO_6. (Note that equation (8) only gives the criteria for a gap closing. The difference between the two sides of equation (8) does *not* give the value of the remaining gap.)

The triplet dispersion for the full model with all tight-binding parameters is shown in Fig.7. The lowest energy triplet excitations occurs along X-W approximately 20 meV below the spin-orbit gap of 350 meV. Although superexchange interactions do reduce the energy cost for magnetic condensation, this 20 meV reduction in energy is very small compared to the overall spin-orbit gap of 350 meV. Consequently magnetic condensation is extremely unfavorable.

B. Magnetism from antisite disorder

Since the absence of magnetism in d^4 Mott insulators can be understood at the atomic level, it would seem that antisite disorder would not alter the picture. While the effects of interactions between B' sites in $A_2BB'O_6$ is unlikely to generate a magnetic state, the situation is different when some B sites also contain d^4 ions. First, the tight-binding values (t) become much larger due to the increased overlap of orbitals between sites. Hence the superexchange interaction strength, $J_{\mathrm{SE}} \sim t^2/U$, becomes significantly larger. This changes the relative strength of J_{SE}/λ which determines if the condensation of magnetic excitations becomes energetically favorable. Second, the orbital geometry now consists of corner sharing octahedra with two active orbitals along a bond in constrast to the FCC lattice where only one orbital primarily contributes to superexchange through t_{33}. With twice as many orbitals, there are four times as many superexchange processes involved, and hence magnetic interactions become much stronger. With both of these contributions, the picture of local non-magnetic singlets will likely break down when both B and B' site contain Ir^{5+} ions. In this situation, the Curie moment from bulk susceptibility scales with the number of B sites containing Ir^{5+} ions.

In the limit that these misplaced ions are isolated antisite defects (with no clustering of misplaced ions), the total susceptibility is then proportional to the number of antisite defects.

$$\chi \propto \frac{j(j+1)g^2\mu_B^2}{3k_B(T-\theta)} \times f_{\mathrm{misplaced}} \qquad (9)$$

Here $f_{\mathrm{misplaced}}$ is the fraction of Ir^{5+} ions appearing on B sites. As a rough estimate, assume that for each misplaced ion, the misplaced ion and its six surrounding B' neighbors become magnetic $j = 1$ states with a corresponding $g = 1/2$. Then the effective Curie moment from bulk susceptibility is given as $\mu_{\mathrm{expt}}^2 = \frac{7}{2}\mu_B^2 \times f_{\mathrm{misplaced}}$. In this scenario, even when just 1 percent of the sites were disordered, the measured bulk μ_{eff} would be $0.18\mu_B$. Although this estimate serves as an upper bound, it shows that the effects of antisite disorder can amount to a substantial contribution.

V. DISCUSSION

There are two different reports on the physical properties of Ba_2YIrO_6 single crystals. Zhang et al. concluded that their Ba_2YIrO_6 single crystals order antiferromagnetically below 1.6 K by measuring specific heat and magnetic properties.[13] In the paramagnetic state, the Curie-Weiss fitting of the magnetic susceptibility in the temperature range $50\,\mathrm{K} \le T \le 300\,\mathrm{K}$ gives an effective moment of $1.44\mu_{\mathrm{B}}$/Ir and a Weiss constant of -149 K. In contrast, Dey et al. did not observe any long range magnetic order for temperatures down to 0.4 K in their crystals.[9] The Curie-Weiss fitting of the magnetic susceptibility in the temperature range $15\,\mathrm{K} \le T \le 300\,\mathrm{K}$ gives an effective moment of $0.44\mu_{\mathrm{B}}$/Ir and a Weiss constant of -8.9 K. Both values are much smaller than those reported by Zhang et al. Our Ba_2YIrO_6 crystals are similar to what Dey et al. obtained with similar χ_0 and θ.

The Curie-Weiss fitting of magnetic susceptibility shown in Fig. 4 gives a χ_0 around 5×10^{-4} emu/mol. This value agrees well with $\chi_0 = 5.83\times10^{-4}$ emu/mol reported by Dey et al.[9] However, all our Ba_2YIrO_6 crystal have an effective moment larger than $0.44\,\mu_{\mathrm{B}}$/Ir reported by Dey et al. Dey et al. did not report the cooling rate during crystal growth. As discussed later, both the cooling rates during and after crystal growth affect the magnetic properties of Ba_2YIrO_6 crystals. The different growth parameters might account for the slight discrepancy in the magnitude of effective moments.

As shown in Figs. 4 and 5, BYIO-16d has a larger effective moment and saturation moment than BYIO-4d and BYIO-4d-Q. The magnetic moment for BYIO-4d-Q is slightly smaller than that of BYIO-4d. The crystal characterization presented in Sec. III-A suggests that the lattice defects should be an important, if not the only, factor affecting the magnetic properties of Ba_2YIrO_6 crystals cooled differently. The observation of clusters of antisite disorder (see Fig. 2(e)) and a larger magnetic moment (see Figs. 4 and 5) in BYIO-16d crystals suggests that antisite disorder favors the formation of magnetic moments out of the $J = 0$ ground state. This is supported by our theoretical analysis. Inside of the antisite disordered clusters, the interactions are enhanced by increased overlap of orbitals between sites and increased number of orbitals mediating. The enhanced magnetic interactions, if strong enough, can break down the picture of local non-magnetic singlets and thus induce condensation of magnetic excitations.

The moment induced by antisite disorder is unexpected considering the detrimental effect of antisite disorder on the magnetic properties of double perovskites. For double perovskites with both B and B' cations magnetic, it has been demonstrated that antisite disorder suppresses the ordered moment, ordering temperature, or coervicity.[22,23] For double perovskites which contain only one magnetic cation but show long range magnetic order, we would expect similar effect since antisite disorder would disturb the magnetic interactions. From this point of view, Ba_2YIrO_6 provides a special case where antisite disorder is beneficial to magnetic moments. This unique feature is rooted in the importance role of interactions in the moment formation of d^4 systems. The occupation of Y site by Ir enhances the interactions thus leading to the appearance of finite-spin Ir ions in their localization volume.

It is interesting to notice that the BYIO-4d-Q sample, in which stripe-like antiphase boundary up to 100 nm is observed in atomic mapping, has a slightly smaller effective moment than the slow cooled BYIO-4d. This suggests that the formation of antiphase boundary reduces the magnetic moment of Ba_2YIrO_6. As shown in Fig. 2(i), the intensity of Ir columns is unchanged while that of Y increases in the antiphase boundary region. The intensity change signals some occupation of Ir at Y site forming an Ir-rich region with a composition of $Ba_2(Y_{1-x}Ir_x)IrO_6$. One important result of this is the appearance of magnetic Ir^{4+} ions with five electrons which are expected to enhance the magnetic moment of Ba_2YIrO_6. This is opposite to the experimental results that BYIO-4d-Q has smaller saturation and effective moments than the slow-cooled BYIO-4d. The intensity profile shown in Fig. 2(i) still suggests an atomic arrangement of Ba-Y-Ba-Ir-Ba. We thus look at the magnetic properties of high pressure cubic phase of $Ba_3YIr_2O_9$ in order to understand the slightly reduced moment in BYIO-4d-Q. $Ba_3YIr_2O_9$ can be stabilized in a cubic (space group Fm-$3m$) structure with an ordered arrangement of IrO_6 and $Y_{2/3}Ir_{1/3}O_6$ octahedra forming the cubic double perovskite $Ba_2Ir(Y_{2/3}Ir_{1/3})O_6$ structure.[24] No long range magnetic order was observed above 2 K for the high pressure cubic phase. The effective moment is reported to be $0.19\mu_B$/Ir, much smaller than $0.50\mu_B$/Ir for BYIO-4d-Q. According to the first-principles study by Panda et al., the magnetic exchange interactions is weak in the cubic $Ba_3YIr_2O_9$ and spin-orbit coupling dominates leading to a quantum spin-orbit liquid state.[25]

Our experimental study and theoretical analysis support the contribution of antisite disorder to the enhanced moment in BYIO-16d. While the Ir-rich antiphase boundary seems to be detrimental to the magnetic moment despite of the formation of $J = 1/2$ Ir ions. Then what is the origin of the observed moment in the slow cooled BYIO-4d? Since the Curie-Weiss-like paramagnetic behavior is observed by various groups in Ba_2YIrO_6 in both single crystal and polycrystalline samples, accidental magnetic impurity by itself is unlikely to account for the observed paramagnetism. While this work does not mean to attribute this solely to antisite disorder or any other mechanism previously proposed by other groups, we want to point out the following:

(1) We would expect some isolated antisite disorder in all Ba_2YIrO_6 crystals grown in this work. This kind of antisite disorder cannot be observed by atomic mapping in STEM study. Based on the simplified estimation discussed in Sec. IV B, only 2-3% antisite disorder can account for the observed effective moment. The small fraction of the isolated antisite disorder in small scales may not be well resolved using x-ray or neutron diffraction techniques. Our STEM studies cannot provide a reliable estimation of the population of antiphase boundaries or clusters of antisite disorder. However, only a small fraction could lead to the observed changed.

(2) Lattice defects must be considered when considering possible sources of the observed moments in $J = 0$ compounds. These include nonstoichiometry of both cations and anions, local inhomogeneity, local lattice distortion due to residual stress, foreign inclusions or substitutions, antisite disorder, twinning and other dislocations.

(3) The experimentally observed magnetism can result from multiple lattice defects instead of a single one. Only a small amount of lattice defects is needed to account for the observed moments. The population of each individual type of defect can be below the detection limit of the techniques sensitive to that type of defect. This makes it challenging to identify the real origin of the observed moment and to reveal the intrinsic magnetic properties of Ba_2YIrO_6. Because the type and concentration of defects are quite sensitive to materials processing parameters, it would be essential to correlate the magnetic properties with the materials processing parameters.

Our DFT and effective magnetic Hamiltonian calculations suggest that magnetic condensation is unlikely and the experimentally observed magnetism can be explained by the enhanced magnetic interactions in the antisite disordered regions. However, the effect of local lattice distortion induced by antisite disorder should also be considered. With a coordination number of six, the ionic radius (IR) of Y^{3+} is 0.90 $\AA$, which is much larger than 0.57 $\AA$ for Ir^{5+}. The large IR difference increases the energy cost for the formation of antisite disorder. It also leads to significant local lattice distortion. As in the case of Sn-doped $SrIrO_3$, the local lattice distortion can partially quench the orbital angular momentum, thus restoring the spin moment.[26]

The sensitivity of magnetism to lattice defects in Ba_2YIrO_6 resembles that in $LaCoO_3$. The thermally driven spin-state transition in $LaCoO_3$, due to a comparable crystal field splitting and Hund exchange energy, have attracted attention for over 50 years. The spin state transition takes place around 100K above which high spin (HS, electronic configuration of t^4e^2) and/or intermediate spin (IS, t^5e^1) states are populated in the low spin (LS, t^6e^0) matrix. The spin state transition is accompanied with a quick drop of magnetic susceptibility upon cooling. Once all Co(III) ions settle in the LS configuration at low temperature, a temperature independent magnetic susceptibility is expected. However, a Curie-like paramagnetic component was observed in all studies below 25K. This low temperature Curie-tail has been postulated to come from paramagnetic impurities, oxygen nonstoichiometry, surface Co(II) ions, or a LS ground state bearing some IS character caused by the virtual excitation to the IS state.[18,27–30] In addition, a ferromagnetic component with Tc∼85 K also contributes to the low temperature magnetism.[31] This ferromagnetism was reported in small single crystals, nano particles, thin films.[32–34] Therefore, the magnetic susceptibility of $LaCoO_3$ in the S=0 state at low temperatures is rather sensitive to lattice defects, crystal surface, twin boundary, local strain field, oxygen vacancies. The strong similarity between Ba_2YIrO_6 and $LaCoO_3$ with respect to the defect induced magnetism suggests that the important effect of lattice defects on local moments is a general phenomenon in $J = 0$ and $S = 0$ compounds. It should be noted that the energy difference between S=0 and S=1 states is only about 16meV for $LaCoO_3$. This small energy difference makes $LaCoO_3$ an ideal system to study the excitonic magnetism.[35–37] In contrast, a large energy gap of 350 meV drives Ba_2YIrO_6 away from the excitonic instability.

VI. SUMMARY

In summary, we investigate the magnetic properties and local defects of three Ba_2YIrO_6 crystals: (1) a slow cooled crystal, (2) a crystal quenched from 900°C, and (3) a crystal that is grown using a faster cooling rate during crystal growth. The atomic imaging by STEM shows that quenching from 900°C introduces antiphase bounaries to the crystals and a faster cooling rate during crystal growth leads to clusters of Y and Ir antisite disorder. The magnetic measurements show that Ba_2YIrO_6 crystals with clusters of antisite disorder have a larger effective moment and a larger saturation moment. The experimental observation indicates the importance of lattice defects in understanding the magnetism in Ba_2YIrO_6.

Our DFT and effective magnetic Hamiltonian calculations suggest the magnetic condensation is unlikely in Ba_2YIrO_6 as the energy to be gained from superexchange is only one quarter of the spin-orbit gap. However, once Y site is taken by Ir in antisite disordered region, the enhanced superexchange interaction, due to increased overlap of orbitals between sites and increased number of orbitals mediating the interactions, is able to overcome the local non-magnetic singlet formation, thereby inducing magnetism. Comparison between $J = 0$ compound Ba_2YIrO_6 and $S = 0$ compound $LaCoO_3$ suggests that the importnant effect of lattice defects on local moments is a general phenomena in $J = 0$ and $S = 0$ compounds.

One key question still remains: Are d^4 systems in the absence of uniaxial distortions and lattice defects still magnetic? In our search for a model system that may harbor novel magnetism in d^4 system, we have found that compared to their Sr-analogs, the Ba oxides are considerably less distorted. However, as shown here the magnetism in the Ba_2YIrO_6 system was nevertheless affected by the lattice defects, such as antisite disorder and antiphase bounadries. We hope that future synthesis of Ba_2YIrO_6 or other related d^4 oxides with minimum amount of lattice defects can explore the predicted novel magnetism with spin-orbit frustration[4]. It would also be useful to explore d^4 systems on pyrochlore geometries which have two active orbitals rather than one in the FCC lattice, thereby enhancing the chances of the condensation mechanism for driving magnetic long range order.

Note: During the preparation of this manuscript, we became aware of the paper by Hammerath et al.[38] which also points to the extrinsic origin of the observed magnetism in Ba_2YIrO_6.

VII. ACKNOWLEDGEMENT

Work at ORNL was supported by the U.S. Department of Energy, Office of Science, Basic Energy Sciences, Materials Sciences and Engineering Division(QZ, BCS, and JQY). CQ, CS, DM, MR, and NT acknowledge the support of the Center for Emergent Materials, an NSF MRSEC, under Award Number DMR-1420451. JSZ was supported by DOD-ARMY (W911NF-16-1-0559). DGM acknowledges the support from the Gordon and Betty Moore Foundations EPiQS Initiative through Grant No. GBMF4416. HDZ acknowledges the support from NSF-DMR 1350002. The STEM experiment in this research was conducted at the ORNLs Center for Nanophase Materials Sciences (CNMS) , which is a DOE Office of Science User Facility.

Appendix A: Matrices $\boldsymbol{A}$, $\boldsymbol{B}$, and $\boldsymbol{C}$

The matrices appearing in equation (6) for H'_{xy} are given explicitly here. The matrices for H'_{yz} and H'_{zx} may be obtained from cyclic permutations of these matrices.

$$\boldsymbol{A} = \frac{1}{U}\begin{pmatrix} t_{11}^2 + \frac{1}{2}t_{33}t_{11} + \frac{2}{3}t_{12}^2 + \frac{1}{6}t_{33}^2 & t_{11}t_{12} - \frac{1}{6}t_{12}t_{33} & 0 \\ t_{11}t_{12} - \frac{1}{6}t_{12}t_{33} & t_{11}^2 + \frac{1}{2}t_{33}t_{11} + \frac{2}{3}t_{12}^2 + \frac{1}{6}t_{33}^2 & 0 \\ 0 & 0 & \frac{2}{3}t_{11}^2 + \frac{1}{3}t_{33}t_{11} + \frac{2}{3}t_{33}^2 \end{pmatrix} \tag{A1}$$

$$\boldsymbol{B} = \frac{1}{U}\begin{pmatrix} -\frac{5}{6}t_{11}^2 - \frac{1}{3}t_{33}t_{11} - \frac{5}{6}t_{12}^2 - \frac{1}{6}t_{33}^2 & \frac{1}{3}t_{12}t_{33} - t_{11}t_{12} & 0 \\ \frac{1}{3}t_{12}t_{33} - t_{11}t_{12} & -\frac{5}{6}t_{11}^2 - \frac{1}{3}t_{33}t_{11} - \frac{5}{6}t_{12}^2 - \frac{1}{6}t_{33}^2 & 0 \\ 0 & 0 & -\frac{2}{3}t_{11}^2 - \frac{2}{3}t_{33}^2 \end{pmatrix} \tag{A2}$$

$$\boldsymbol{C} = \frac{1}{U}\begin{pmatrix} -\frac{5}{18}t_{11}^2 - \frac{1}{9}t_{33}t_{11} + \frac{1}{6}t_{12}^2 + \frac{1}{18}t_{33}^2 & -\frac{1}{3}t_{11}t_{12} - \frac{1}{3}t_{33}t_{12} & 0 \\ -\frac{1}{3}t_{11}t_{12} - \frac{1}{3}t_{33}t_{12} & -\frac{5}{18}t_{11}^2 - \frac{1}{9}t_{33}t_{11} + \frac{1}{6}t_{12}^2 + \frac{1}{18}t_{33}^2 & 0 \\ 0 & 0 & \frac{2}{9}t_{11}^2 - \frac{4}{9}t_{33}t_{11} - \frac{1}{9}t_{33}^2 \end{pmatrix} \tag{A3}$$

Appendix B: Inclusion of next-nearest neighbors

Without going through further formalism, we can estimate the effect of including both nearest neighbor (NN) and next-nearest neighbor (NNN) interactions. Since the NNN Ir ions are in an octahedral configuration around each Ir ion, the NNN case is exactly that of the single perovskite first obtained by Khaliullin. Since the dispersions of the NN and NNN interactions add linearly for each triplet excitation type, $\omega(\boldsymbol{k}) = \omega_{\mathrm{NN}}(\boldsymbol{k}) + \omega_{\mathrm{NNN}}(\boldsymbol{k})$, we can put an upper bound on the result by constructively adding the two energy scales together

$$\frac{16}{3}\frac{t_{33}^2}{U} + 10\frac{t_{\mathrm{NNN}}^2}{U} \geq \Delta_{\mathrm{SOC}} \tag{B1}$$

where the relevant NNN tight-binding parameter obtained from our DFT calculation is $t_{\mathrm{NNN}} = -18$ meV. This contributes an extra 2 meV on the left hand side of (B1), and it only amounts to 47 meV instead of the original 45 meV estimate given in the main text.

---

[*] trivedi.15@osu.edu
[†] yanj@ornl.gov

[1] A. Earnshaw, B. Figgis, J. Lewis, and R. Peacock, Journal of the Chemical Society (Resumed) , 3132 (1961).
[2] G. Cao, T. Qi, L. Li, J. Terzic, S. Yuan, L. E. DeLong, G. Murthy, and R. K. Kaul, Physical review letters **112**, 056402 (2014).
[3] G. Khaliullin, Physical review letters **111**, 197201 (2013).
[4] O. N. Meetei, W. S. Cole, M. Randeria, and N. Trivedi, Physical Review B **91**, 054412 (2015).
[5] S. Bhowal, S. Baidya, I. Dasgupta, and T. Saha-Dasgupta, Physical Review B **92**, 121113 (2015).
[6] K. Pajskr, P. Novák, V. Pokornỳ, J. Kolorenč, R. Arita, and J. Kuneš, Physical Review B **93**, 035129 (2016).
[7] B. F. Phelan, E. M. Seibel, D. Badoe, W. Xie, and R. Cava, Solid State Communications **236**, 37 (2016).
[8] T. Sato, T. Shirakawa, and S. Yunoki, arXiv preprint arXiv:1603.01800 (2016).
[9] T. Dey, A. Maljuk, D. Efremov, O. Kataeva, S. Gass, C. Blum, F. Steckel, D. Gruner, T. Ritschel, A. Wolter, et al., Physical Review B **93**, 014434 (2016).
[10] B. Ranjbar, E. Reynolds, P. Kayser, B. J. Kennedy, J. R. Hester, and J. A. Kimpton, Inorganic chemistry **54**, 10468 (2015).
[11] L. Corredor, G. Aslan-Cansever, M. Sturza, K. Manna, A. Maljuk, S. Gass, A. Zimmermann, T. Dey, C. Blum, M. Geyer, et al., arXiv preprint arXiv:1606.05104 (2016).
[12] Z. Zhao, S. Calder, A. Aczel, M. McGuire, B. Sales, D. Mandrus, G. Chen, N. Trivedi, H. Zhou, and J.-Q. Yan, Physical Review B **93**, 134426 (2016).
[13] H. Zhang, J. Terizc, F. Ye, P. Schlottmann, H. Zhao, S. Yuan, and G. Cao, arXiv preprint arXiv:1608.07624 (2016).
[14] J. Wang, J. Terzic, T. Qi, F. Ye, S. Yuan, S. Aswartham, S. Streltsov, D. Khomskii, R. K. Kaul, and G. Cao, Physical Review B **90**, 161110 (2014).
[15] M. Laguna-Marco, P. Kayser, J. Alonso, M. Martínez-Lope, M. van Veenendaal, Y. Choi, and D. Haskel, Physical Review B **91**, 214433 (2015).
[16] O. Krivanek, G. Corbin, N. Dellby, B. Elston, R. Keyse, M. Murfitt, C. Own, Z. Szilagyi, and J. Woodruff, Ultramicroscopy **108**, 179 (2008).
[17] B. Esser, A. Hauser, R. Williams, L. Allen, P. Woodward, F. Yang, and D. McComb, Physical review letters **117**, 176101 (2016).
[18] J.-Q. Yan, J.-S. Zhou, and J. Goodenough, Physical Review B **69**, 134409 (2004).
[19] European Synchrotron Radiation Facility experimental report, Resonant inelastic x-ray scattering of the new iridium compound Ba2YIrO6.2015.
[20] P. Blaha, K. Schwarz, G. Madsen, D. Kvasnicka, and J. Luitz, An augmented plane wave+ local orbitals program for calculating crystal properties (2001).
[21] A. A. Mostofi, J. R. Yates, G. Pizzi, Y.-S. Lee, I. Souza, D. Vanderbilt, and N. Marzari, Computer Physics Communications **185**, 2309 (2014).
[22] T.-W. Lim, S.-D. Kim, K.-D. Sung, Y.-M. Rhyim, H. Jeen, J. Yun, K.-H. Kim, K.-M. Song, S. Lee, S.-Y. Chung, et al., Scientific reports **6**, 19746 (2016).
[23] J. Navarro, M. Bibes, A. Roig, B. Martinez, and J. Fontcuberta, Applied Physics Letters **78**, 781 (2001).
[24] T. Dey, A. Mahajan, R. Kumar, B. Koteswararao, F. Chou, A. Omrani, and H. Ronnow, Physical Review B **88**, 134425 (2013).
[25] S. Panda, S. Bhowal, Y. Li, S. Ganguly, R. Valentí, L. Nordström, and I. Dasgupta, Physical Review B **92**, 180403 (2015).
[26] Q. Cui, J.-G. Cheng, W. Fan, A. E. Taylor, S. Calder, M. A. McGuire, J.-Q. Yan, D. Meyers, X. Li, Y. Cai, et al., Physical review letters **117**, 176603 (2016).
[27] M. Senarıs-Rodrıguez and J. Goodenough, Journal of Solid State Chemistry **118**, 323 (1995).
[28] C. He, H. Zheng, J. Mitchell, M. Foo, R. Cava, and C. Leighton, Applied Physics Letters **94**, 102514 (2009).
[29] D. Fuchs, C. Pinta, T. Schwarz, P. Schweiss, P. Nagel, S. Schuppler, R. Schneider, M. Merz, G. Roth, and H. v. Löhneysen, Physical Review B **75**, 144402 (2007).
[30] S. Giblin, I. Terry, S. Clark, T. Prokscha, D. Prabhakaran, A. Boothroyd, J. Wu, and C. Leighton, EPL (Europhysics Letters) **70**, 677 (2005).
[31] J.-Q. Yan, J.-S. Zhou, and J. Goodenough, Physical Review B **70**, 014402 (2004).
[32] F. Rivadulla, Z. Bi, E. Bauer, B. Rivas-Murias, J. M. Vila-Fungueirino, and Q. Jia, Chemistry of Materials **25**, 55 (2012).
[33] A. Harada, T. Taniyama, Y. Takeuchi, T. Sato, T. Kyomen, and M. Itoh, Physical Review B **75**, 184426 (2007).
[34] S. Zhou, L. Shi, J. Zhao, L. He, H. Yang, and S. Zhang, Physical Review B **76**, 172407 (2007).
[35] J. F. Afonso and J. Kuneš, Physical Review B **95**, 115131 (2017).
[36] M. Altarawneh, G.-W. Chern, N. Harrison, C. Batista, A. Uchida, M. Jaime, D. Rickel, S. Crooker, C. Mielke, J. Betts, et al., Physical review letters **109**, 037201 (2012).

[37] A. Ikeda, T. Nomura, Y. H. Matsuda, A. Matsuo, K. Kindo, and K. Sato, Physical Review B **93**, 220401 (2016).

[38] F. Hammerath, R. Sarkar, S. Kamusella, C. Baines, H.-H. Klauss, T. Dey, A. Maljuk, S. Ga, A.U.B. Wolter, H.-J. Grafe, S. Wurmehl, B. Bchner. Diluted paramagnetic impurities in nonmagnetic Ba2YIrO6. arxiv:1706.06027.